

Impulsive alignment of $^4\text{He-CH}_3\text{I}$: A theoretical study

Cite as: J. Chem. Phys. **149**, 124301 (2018); <https://doi.org/10.1063/1.5048338>

Submitted: 13 July 2018 . Accepted: 31 August 2018 . Published Online: 24 September 2018

Patricia Vindel-Zandbergen, Ji Jiang, Marius Lewerenz, Christoph Meier, Manuel Barranco, Martí Pi, and Nadine Halberstadt 



View Online



Export Citation



CrossMark

ARTICLES YOU MAY BE INTERESTED IN

[Communication: State-to-state inelastic scattering of interstellar \$\text{O}_2\$ with \$\text{H}_2\$](#)

The Journal of Chemical Physics **149**, 121101 (2018); <https://doi.org/10.1063/1.5051610>

[Parent bending effects on nonadiabatic transition dynamics: Isotopomer-resolved imaging of photodissociation of \$\text{CF}_3\text{Br}\$ at two source temperatures](#)

The Journal of Chemical Physics **149**, 124303 (2018); <https://doi.org/10.1063/1.5047927>

[Femtosecond laser induced Coulomb explosion imaging of aligned OCS oligomers inside helium nanodroplets](#)

The Journal of Chemical Physics **149**, 154306 (2018); <https://doi.org/10.1063/1.5049555>



Impulsive alignment of $^4\text{He}-\text{CH}_3\text{I}$: A theoretical study

Patricia Vindel-Zandbergen,^{1,a)} Ji Jiang,² Marius Lewerenz,² Christoph Meier,¹
Manuel Barranco,^{1,3,4} Martí Pi,^{3,4} and Nadine Halberstadt^{1,b)}

¹Laboratoire Collisions Agrégats Réactivité (LCAR), IRSAMC, Université de Toulouse, CNRS UMR 5589, Toulouse, France

²Laboratoire de Modélisation et Simulation Multi Echelle, Equipe de Chimie Théorique,

5 Boulevard Descartes 77454, Marne-la Vallée Cedex 2, France

³Departament FQA, Facultat de Física, Universitat de Barcelona, Barcelona, Spain

⁴Institute of Nanoscience and Nanotechnology (IN²UB), Universitat de Barcelona, Barcelona, Spain

(Received 13 July 2018; accepted 31 August 2018; published online 24 September 2018)

We simulate the non-adiabatic laser alignment of the weakly bound $^4\text{He}-\text{CH}_3\text{I}$ complex based on a quantum mechanical wave packet calculation for a model $\text{He}-\text{CH}_3\text{I}$ interaction potential. Two different regimes are found depending on the laser intensity. At intensities typical of non-adiabatic alignment experiments, the rotational dynamics resembles that of the isolated molecule. This is attributed to the fact that after the initial prompt alignment peak the complex rapidly dissociates. The subsequent revival pattern is due to the free rotation of the molecule detached from the helium atom. It is superimposed to a flat background corresponding to $\sim 20\%$ of the wave packet which remains bound, containing lower rotational excitation. At lower intensities, dissociation is avoided but the rotational excitation is not high enough to provide an efficient alignment and a broad non-regular structure is observed. Besides, the interaction of the He atom with the molecule quenches any possible alignment. These interpretations are based on the calculation of different observables related to the rotational motion. We compare our findings with recent experimental and theoretical results of non-adiabatic alignment of linear molecules solvated in helium nanodroplets or weakly interacting with one helium atom. *Published by AIP Publishing.* <https://doi.org/10.1063/1.5048338>

I. INTRODUCTION

The alignment of molecular species by intense non-resonant laser fields has been widely studied both experimentally and theoretically within the last two decades.¹ It has proven to be very useful in many applications in molecular science.²⁻⁷ Laser-induced alignment in the non-adiabatic regime where the laser pulse is turned on (and off) much faster than the rotational period of the molecule, $\tau_{\text{pulse}} < \tau_{\text{rot}}$, is well understood.⁸⁻¹⁰ The strong pulse interaction leaves the system aligned after the turn-off as the result of a coherent superposition of a large number of rotational levels. The subsequent dynamics is then driven by the time evolution of the free rotor states. At short times, it exhibits strong dephasing at a rate proportional to the square of the wave packet width in J -space, leading to an almost isotropic orientational distribution. However, for an isolated system, due to the discreteness of the spectrum and to the finite number of excited rotational states involved, the rotational wave packet rephases at well-defined time intervals, leading to the same aligned state as the one at the end of the laser pulse (rotational revivals).^{9,11} Hence, non-adiabatic alignment has the advantage of providing a field free alignment of molecules at these predetermined times of the revivals and survives for a controllable period.^{12,13}

Most of the research so far has dealt with the alignment of isolated molecules in the gas phase. However, since the phenomena of revivals depend crucially on the coherent evolution of the rotational wave packet, it provides a sensitive tool to study the interaction with a weakly interacting environment. Along this line, more recent studies are focusing on the alignment of molecules that interact with one another, weakly bound molecular systems involving van der Waals bonds, or molecules coupled to an environment in the solid or liquid phase.¹⁴⁻²¹ Laser induced alignment of molecules in a liquid is hindered by several mechanisms which are absent in vacuum. In a classical solvent, molecular rotation is not free due to the molecular forces exerted by the surrounding environment. In addition, the molecules of the solvent may be polarized or even ionized, which can alter any alignment created, as can collisions with molecules of the solvent. Superfluid helium nanodroplets constitute an interesting alternative. They are characterized by their ability to solvate almost any molecule and exhibit a very low polarizability and a high ionization potential, which minimizes any interaction with the laser light. In addition, a discrete rotational structure has been observed in high resolution infrared and microwave spectroscopies, which was taken as a proof of their superfluidity.²²⁻²⁵ Due to these properties, superfluid He is expected to be an advantageous environment for laser induced alignment.

Recent time-resolved experiments have shown that moderately intense laser pulses can induce alignment of molecules

^{a)}Electronic mail: patricia.vindel@irsamc.ups-tlse.fr

^{b)}Electronic mail: Nadine.Halberstadt@irsamc.ups-tlse.fr

inside He nanodroplets.^{26–28} However, the measurements revealed a different dynamics from that of gas phase molecules, contrary to what could have been expected from superfluid motion. The initial alignment dynamics was much slower than for isolated species and the transient alignment recurrences (revival pattern) characteristic of gas phase molecules were absent. New experiments on impulsive alignment of iodine molecules inside He nanodroplets²⁹ showed that it is possible to create a coherent rotational wave packet lasting long enough to form revivals, and that at high laser fluences initial alignment dynamics can be as fast as for isolated molecules. The mechanism behind these results has been theoretically described within the angulon quasiparticle approach.³⁰ The authors propose that the rotational dynamics is due to the rotation of the iodine molecules together with a helium solvation shell.

Recent theoretical work has studied the non-adiabatic alignment of a van der Waals complex of linear molecules and one single He atom by numerically solving the time dependent Schrödinger equation.³¹ Two different regimes were found depending on the laser intensity. At intensities typical of non-adiabatic alignment, the rotational dynamics resembles that of isolated molecules; however, the complexes rapidly dissociate. At lower intensities, in the non-dissociative regime, a non-regular and continuously evolving structure is seen.

Motivated by these experimental and theoretical results, we present a quantum dynamical analysis of the non-adiabatic alignment and subsequent rotational motion of the van der Waals complex formed with the CH₃I molecule and a single He atom, based on the solution of the time dependent Schrödinger equation using a model ⁴He–CH₃I interaction potential. Emphasis is put on the effect of the helium atom on the coherent time evolution of the rotor states. We gain insight in the alignment dynamics by analyzing the time-dependent wave packet. Our main finding is that for laser pulse intensities needed to induce alignment in gas phase, the ⁴He–CH₃I complex mostly dissociates as observed in Ref. 31. The initial rotational dynamics coincides with that of an isolated molecule, and the observed revival pattern is due to the alignment of CH₃I coming from the dissociated complex, superimposed to a broadly oscillating background coming from the part of the wave packet that remains bound. For lower intensities, dissociation is avoided, but no efficient alignment is achieved and the interaction of the He atom with the molecule quenches any possible alignment. The possible consequences of these findings in the context of helium nanodroplets are sketched out.

II. THEORY

A. Quantum dynamics of the ⁴He–CH₃I van der Waals complex

We present a theoretical and numerical study of the non-adiabatic alignment of the van der Waals complex formed by CH₃I and a single helium atom based on the solution of the time-dependent Schrödinger equation. The degrees of freedom included are the overall rotation of the complex, the CH₃I rotation, and the helium motion. The latter can range from

bound (stretching and bending vibrations) to free, dissociated (translation and rotation) motion. The complete Hamiltonian of the system is

$$H(t) = H_{\text{mol}} + H_{\text{las}}(t), \quad (1)$$

where H_{mol} is the field-free molecular Hamiltonian and H_{las} is the Hamiltonian for the laser-complex interaction. For non-adiabatic alignment, the laser-matter interaction is non-resonant and it is given by¹

$$H_{\text{las}}(t) = -\frac{1}{4} \sum_{\rho} \mathcal{E}_{\rho}(t) \mu_{\rho}^{\text{ind}} = -\frac{1}{4} \sum_{\rho, \rho'} \mathcal{E}_{\rho} \alpha_{\rho \rho'} \mathcal{E}_{\rho'}^*, \quad (2)$$

where $\rho, \rho' = X, Y, Z$ are the space-fixed (SF) Cartesian coordinates, \mathcal{E}_{ρ} are the Cartesian components of the electric field, α is the polarizability tensor, and μ^{ind} is the induced dipole operator approximated by that of CH₃I.

In the case of a symmetric top molecule, H_{las} simplifies to³²

$$H_{\text{las}}(t) = -\frac{1}{4} \mathcal{E}^2(t) \Delta \alpha \cos^2 \theta, \quad \Delta \alpha = \alpha_{\parallel} - \alpha_{\perp}, \quad (3)$$

where α_{\parallel} and α_{\perp} are the components of the polarizability tensor parallel and perpendicular to the molecular symmetry axis, respectively, and θ is the angle between the polarization axis of the laser field and the symmetry axis of the molecule.

The pulse intensity $I(t) = c \epsilon_0 \mathcal{E}^2(t)$ is modeled as

$$I(t) = \begin{cases} I_0 \sin^4(\pi t/\tau) & \text{if } 0 \leq t \leq \tau \\ 0 & \text{otherwise,} \end{cases} \quad (4)$$

with I_0 being the peak intensity and τ being the total pulse duration, this form ensuring that the pulse will be strictly zero outside the $[0, \tau]$ time interval.

In order to simplify the calculations, CH₃I is approximated by a diatomic molecule. This is justified by the fact that $A \gg B$ where A is the constant for rotation about the C₃ C–I axis and B is the constant for rotation about an axis perpendicular to it: $A = 155\,092.4$ MHz ($5.173\,325\,6$ cm⁻¹), while $B = 7\,501.275\,745\,6$ MHz ($0.250\,215\,62$ cm⁻¹).³³ With these values, the Boltzmann population of the symmetric top rotational levels (J, K) with $K > 0$ (K being the projection quantum number of \mathbf{J} on the C–I symmetric top axis) is negligible at the helium droplet temperature of 0.4 K. In addition, the CH₃I dipole moment is along the C–I axis; hence, alignment dynamics does not involve rotation about the C–I axis.

Within the rigid rotor approximation, H_{mol} then reduces to

$$H_{\text{mol}} = H_{\text{rot}} + V(R, \theta^{BF}) + T_R. \quad (5)$$

In this equation, the helium atom is described within the body fixed (BF) frame (x, y, z) illustrated in Fig. 1: its z axis is parallel to the C–I bond and its x axis lies in the plane defined by the C–I bond and the helium atom. \mathbf{R} is the Jacobi coordinate from the center of mass of CH₃I to the He atom, with spherical coordinates $(R, \theta^{BF}, \varphi^{BF} = 0)$, with $\theta^{BF} = 0$ at the iodine side. The origin is set at the center of mass of the system; hence, the radial part of the kinetic energy is given by $T_R = -(\hbar^2/2\mu)\nabla_R^2$, with $\mu = m_{\text{He}}m_{\text{CH}_3\text{I}}/(m_{\text{He}} + m_{\text{CH}_3\text{I}})$ being the reduced mass of the complex.

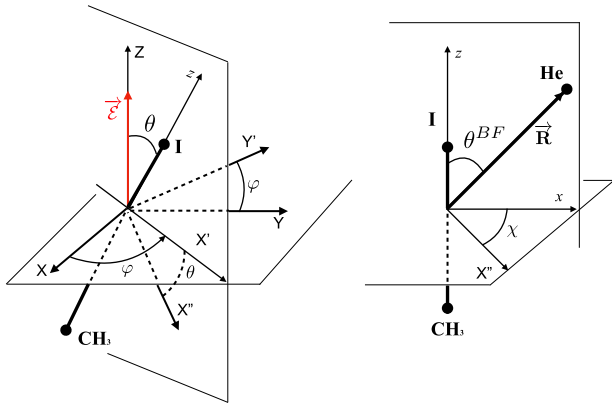


FIG. 1. Coordinates and reference frames used in this work. (X, Y, Z) is a space-fixed (SF) frame with its Z axis parallel to the electric field \vec{E} of the laser pulse. (x, y, z) is the body-fixed (BF) frame with its z axis parallel to the C–I axis and with the x axis such that the He atom is in the (x, z) plane. The Euler angles for rotating from the SF to the BF frame³⁴ are represented on the left plot (φ, θ) or on the right plot (χ). θ is also the alignment angle between the C–I axis and the electric field. \mathbf{R} is the vector going from the center of mass of CH_3I and the He atom, with θ^{BF} being its angle with the BF z axis.

The ^4He – CH_3I interaction potential $V(R, \theta^{BF})$ is described later in Sec. II B, and the rotational Hamiltonian H_{rot} (angular kinetic energy of the molecule and of the helium atom) is given by

$$H_{\text{rot}} = \frac{B}{\hbar^2} \mathbf{j}^2 + \frac{\mathbf{l}^2}{2\mu R^2}, \quad (6)$$

with \mathbf{j} being the angular momentum of CH_3I about its center of mass and \mathbf{l} being the angular momentum of the orbital motion of the helium atom and the center of mass of the molecule about their common center of mass. Here, $B = \hbar^2/2I$ is the CH_3I rotational constant with I being the moment of inertia of the CH_3I molecule about an axis perpendicular to the C–I axis.

We introduce the total angular momentum of the complex $\mathbf{J} = \mathbf{j} + \mathbf{l}$, with projection J_Z on the space-fixed Z axis and J_z on the body-fixed z axis. The wave function Ψ is expanded in the coupled body-fixed (BF) eigenbasis $|JMI\Omega\rangle$ of $\mathbf{J}^2, J_Z, \mathbf{l}^2, l_z,$ and J_z . Note that in the case of a diatomic molecule, the projection of \mathbf{j} on the BF z axis is $j_z = 0$, and thus $J_z = l_z$. Using this basis, the total wave function is expanded as

$$\Psi(t) = \sum_{J'M'l'\Omega'} C_{J'M'l'\Omega'}(R, t) |J'M'l'\Omega'\rangle, \quad (7)$$

where the basis functions are

$$|n\rangle = |JMI\Omega\rangle = \sqrt{\frac{2J+1}{8\pi^2}} D_{M\Omega}^{*J}(\varphi, \theta, \chi) \Theta_{l\Omega}(\theta^{BF}). \quad (8)$$

In this expansion, φ, θ, χ are the Euler angles for the body fixed (CH_3I) axes (x, y, z) with respect to the space-fixed axes (X, Y, Z) illustrated in Fig. 1; θ^{BF} is the angle of the He atom with respect to the z axis in the body fixed frame; $D_{M\Omega}^J$ are the Wigner rotation matrices⁵³ and $\Theta_{l\Omega}(\theta^{BF})$ are $\varphi^{BF} = 0$ spherical harmonics proportional to the associate Legendre functions $P_{l\Omega}(\cos \theta^{BF})$, defined by $Y_{l\Omega}(\theta^{BF}, \varphi^{BF}) = \Theta_{l\Omega}(\theta^{BF}) e^{i\Omega\varphi^{BF}} / \sqrt{2\pi}$ with $\varphi^{BF} = 0$.

Substituting Eq. (7) into the time-dependent Schrödinger equation and projecting onto the $|n\rangle = |JMI\Omega\rangle$ state yields

the following set of coupled equations for the expansion coefficients:

$$\begin{aligned} i\hbar \dot{C}_n(R, t) &= \sum_{n'} \langle n | H(t) | n' \rangle C_{n'}(R, t) \\ &= -\frac{\hbar^2}{2\mu} \frac{d^2}{dR^2} C_n(R, t) + \sum_{n'} \left[\langle n | \frac{\mathbf{l}^2}{2\mu R^2} | n' \rangle \right. \\ &\quad + \langle n | \frac{B}{\hbar^2} \mathbf{j}^2 | n' \rangle + \langle n | V(R, \theta^{BF}) | n' \rangle + \langle n | H_{\text{las}}(t) | n' \rangle \left. \right] \\ &\quad \times C_{n'}(R, t). \end{aligned} \quad (9)$$

The diagonal matrix elements for the different angular kinetic operators are

$$\langle JMI\Omega | \frac{\mathbf{l}^2}{2\mu R^2} | JMI\Omega \rangle = \frac{\hbar^2 l(l+1)}{2\mu R^2}, \quad (10)$$

$$\langle JMI\Omega | \frac{B}{\hbar^2} \mathbf{j}^2 | JMI\Omega \rangle = B[J(J+1) + l(l+1) - 2\Omega^2], \quad (11)$$

and the non-diagonal elements (Coriolis coupling)

$$\begin{aligned} \langle JMI\Omega | \frac{B}{\hbar^2} \mathbf{j}^2 | JMI(\Omega \pm 1) \rangle &= -B\sqrt{J(J+1) - \Omega(\Omega \pm 1)} \\ &\quad \times \sqrt{l(l+1) - \Omega(\Omega \pm 1)} \end{aligned} \quad (12)$$

with all other matrix elements being zero.

The matrix elements for the interaction⁵⁴ with the laser pulse are given by

$$\begin{aligned} \langle JMI\Omega | H_{\text{las}}(t) | J'M'l'\Omega' \rangle \\ = -\frac{1}{4} \mathcal{E}^2(t) \Delta\alpha \langle JMI\Omega | \cos^2 \theta | J'M'l'\Omega' \rangle \end{aligned} \quad (13)$$

with

$$\begin{aligned} \langle JMI\Omega | \cos^2 \theta | J'M'l'\Omega' \rangle \\ = \delta_{MM'} \delta_{\Omega\Omega'} \delta_{l'l'} (-1)^{\Omega-M} \sqrt{2J+1} \sqrt{2J'+1} \\ \times \begin{pmatrix} J & 2 & J' \\ -M & 0 & M \end{pmatrix} \begin{pmatrix} J & 2 & J' \\ -\Omega & 0 & \Omega \end{pmatrix}. \end{aligned} \quad (14)$$

B. He– CH_3I interaction potential

In order to obtain $V(R, \theta^{BF})$ in Eq. (5), we first determined the ^4He – CH_3I interaction as a sum over a CH_3 –He interaction and a He–I interaction, each one calculated *ab initio*. This is a rather severe approximation since the CH_3I molecule cannot be simply described as the sum of a CH_3 radical and an iodine atom. We believe that the resulting van der Waals interaction is still reasonable, at least concerning the features that are important for this study, for several reasons. The CH_3 electronic orbitals have the correct sp^3 hybridization imposed by the tetrahedral shape. Hence the anisotropy of the interaction, which is essential for the motion of He relative to CH_3I , should be correct. The free orbital resulting from sp^3 hybridization is used to bind to the iodine atom, with the region between C and I being repulsive for the He atom anyway since helium-electron interaction is repulsive. The main error that can be expected from this potential comes from charge transfer from the CH_3 part to the iodine atom, which results in a moderate dipole moment. From the point of view of the He– CH_3I potential, this means that the interaction should be less attractive on the iodine side since iodine is negatively charged, and

more attractive on the CH₃ side which is positively charged. However, the polarizability of the helium atom is small, and the equilibrium position that we obtain is already on the CH₃ side, so that changes will be quantitative but not qualitative: deeper potential well, slightly larger anisotropy. Instead of dissociating for $J \geq 8$ [$B J(J+1) \approx 18 \text{ cm}^{-1}$] as discussed later in this paper, the complex might dissociate for $J \geq 9$ or 10 [$B J(J+1) \approx 22.5$ or 27.5 cm^{-1}], which will not alter the conclusions from this work.

Both components were determined by RCCSD(T) [(spin-)restricted coupled cluster method with full treatment of single and double excitations and perturbative treatment of triple excitations] calculations using the MOLPRO suite of *ab initio* programs³⁵ and least squares fitted to appropriate analytical representations.

For the He–I part, the interaction energies for the two lowest electronic states $^2\Sigma^+$ and $^2\Pi$ arising from the s^2p^5 electronic configuration of the iodine atom were computed using an effective core potential^{36,37} and treating explicitly only the $4s$, $4p$, $4d$, $5s$, and $5p$ electrons of iodine using augmented Dunning basis sets.^{38,39} The $5s$ and $5p$ electrons of iodine and the $1s$ electrons of helium were explicitly treated in the correlation calculations. A radial grid of 47 points densely covering distances from $6a_0$ to $12a_0$ with progressively sparser coverage out to $100a_0$ was explored. The interaction energies obtained at augmented triple, quadruple, and quintuple zeta level were extrapolated to the infinite basis limit⁴⁰ and fitted to an extended Tang-Toennies model $V(r) = A \exp[\beta(r)r] - \sum_k f_k c_k / r^k$ with $\beta(r) = \beta_1 + \beta_2 r$ and $k = 6, 8$ and a Tang-Toennies damping function $f_k(r)$,⁴¹ resulting in a root mean square error of less than 0.05 cm^{-1} . In order to account for the spin-orbit interaction in the iodine atom, the fitted zero order $^2\Sigma^+$ and $^2\Pi$ interactions are used to construct a complex 6×6 matrix using the experimental spin-orbit splitting of 7603.15 cm^{-1} assumed to be independent of the iodine–helium distance. The iodine–helium interaction energy is taken to be the lowest eigenvalue of this matrix.

The three dimensional CH₃–He interaction potential $V(R, \theta', \phi')$ for a given geometry of the CH₃ fragment respecting C_{3v} symmetry is represented with a Hartree-Fock-dispersion (HFD) style functional form⁴² for the radial dependence with parameters which are expressed as expansions over tesseral harmonics $T(\theta', \phi')$,

$$V(R, \theta', \phi') = A \exp \{-b(\theta', \phi')(R - R_e(\theta', \phi'))\} - \frac{C_6(\theta', \phi')}{R^6} - \frac{C_8(\theta', \phi')}{R^8}, \quad (15)$$

$$X(\theta', \phi') = \sum_{lm} x_{lm} T_{lm}(\theta', \phi'), \quad X = b, R_e, C_6, C_8.$$

In the last expansion, l goes from 0 to $l_{max} = 6$ and the allowed m values are $m = 3k$, $k = 0, 1, \dots$ and $m \leq l$. In this section, θ' is the angle between the vector \mathbf{R} and the symmetry axis of CH₃ with $\theta' = 0$ corresponding to helium on the carbon side of pyramidal CH₃, and ϕ' is the azimuthal angle for rotation of \mathbf{R} around this axis with $\phi' = 0$ corresponding to helium being in a plane containing a hydrogen atom.

The condition $V(R, \theta', \phi') = V(R, \theta', -\phi')$ arising from the rotational symmetry of the potential eliminates tesseral harmonics with a sine factor from the angular basis which is

thereby limited to

$$T_{lm}(\theta', \phi') = \sqrt{2} N_{lm} P_{lm}(\cos \theta') \cos m\phi', \quad m > 0,$$

$$T_{l0}(\theta', \phi') = N_{l0} P_{l0}(\cos \theta'), \quad (16)$$

$$N_{lm} = \left(\frac{2l+1}{4\pi} \frac{(l-m)!}{(l+m)!} \right)^{1/2},$$

and $P_{lm}(\cos \theta')$ is an associate Legendre function.⁴³

The *ab initio* interaction energies underlying this analytical representation were obtained by counterpoise corrected RCCSD(T) calculations using augmented quadruple zeta basis sets for all atoms. The radial grid ranged from 2.9 to 10 Å and the angles θ' and ϕ' were explored on grids with a spacing of $\pi/12$ using the ranges $0 \leq \theta' \leq \pi$ and $0 \leq \phi' \leq \pi/3$. Only interaction energies below $+50 \text{ cm}^{-1}$ were used in the least squares fit representing 963 data points out of a total of 1108. Since the higher order expansion parameters for C_8 were statistically not well determined, the final fitting model used only $l_{max} = 4$ for the C_8 expansion leading to a total of 42 free fitting parameters which represent the *ab initio* data within a root mean square error of 0.1 cm^{-1} .

C. Potential matrix elements

The interaction potential obtained above is then averaged over φ^{BF} (or ϕ') and expanded in $\varphi^{BF} = 0$ spherical harmonics $\Theta_{\lambda 0}(\theta^{BF})$ defined in the text following Eq. (8) as^{44,45}

$$V(R, \theta^{BF}) = \sum_{\lambda} \sqrt{\frac{2}{2\lambda+1}} v_{\lambda 0}(R) \Theta_{\lambda 0}(\theta^{BF}). \quad (17)$$

Its matrix elements are

$$\langle n | V(R, \theta^{BF}) | n' \rangle = \sum_{\lambda} (-1)^{\Omega-M} \left(\frac{(2l+1)(2l'+1)(2\lambda+1)}{2} \right)^{\frac{1}{2}} \times v_{\lambda 0}(R) \begin{pmatrix} l & \lambda & l' \\ -M & 0 & M' \end{pmatrix} \begin{pmatrix} l & \lambda & l' \\ -\Omega & 0 & \Omega' \end{pmatrix} \times \delta_{MM'} \delta_{\Omega\Omega'} \delta_{JJ'}. \quad (18)$$

Figure 2(a) shows the averaged ground state interaction potential in the (x, z) plane containing the C–I molecular axis, with the center of mass of the CH₃I molecule placed at the origin. It has a potential well which corresponds to the equilibrium distance of $R_e = 3.97 \text{ Å}$ and angle $\theta_e^{BF} = 0.589 \pi$ (1.85 rad or 106°), with dissociation energy $D_e = 33.5 \text{ cm}^{-1}$ [instead of -37.2 cm^{-1} at $R_e = 3.9 \text{ Å}$, $\theta_e^{BF} = 0.61 \pi$ (109.5°) and $\phi^{BF} = \pi/3$ (between two hydrogen atoms) before averaging].

The $J = 0$ ground and first excited state wave functions are displayed in Figs. 2(b) and 2(c), respectively. The ground state one is localized in the potential well with a rather wide zero-point amplitude in R and θ^{BF} . Its energy is $E = -13.001 \text{ cm}^{-1}$ with respect to the dissociation limit. The ($J = 0$) excited state wave function corresponds to an angular (bending) excitation with its node close to θ_e^{BF} . It is widely delocalized in angle, showing almost free rotation of He around the CH₃I molecule (69% $l = 1$). The corresponding excitation energy with respect to the ground state is $\sim 5.2 \text{ cm}^{-1}$ ($E = -7.837 \text{ cm}^{-1}$).

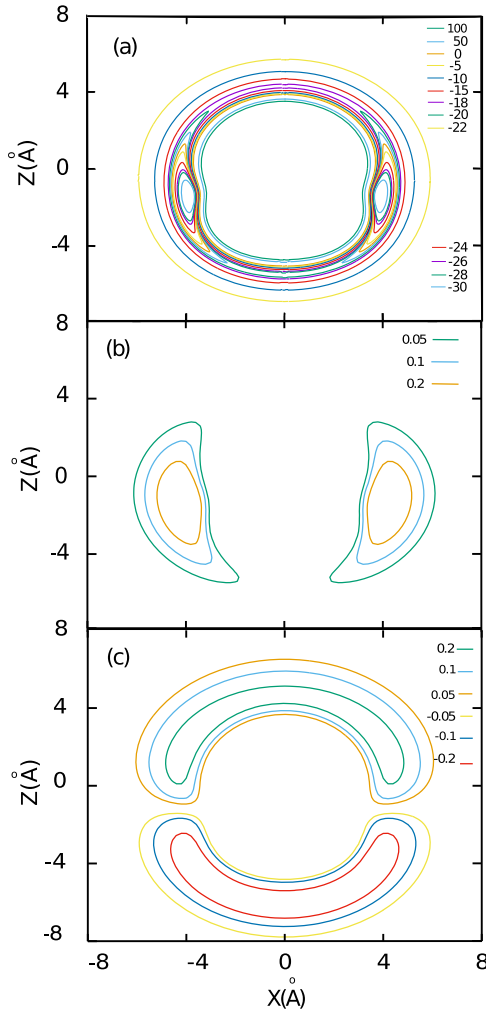


FIG. 2. Contour plots for (a) averaged ground state interaction potential with contour lines for the energy in cm^{-1} , (b) $J = 0$ ground state wave function, $E = -13.001 \text{ cm}^{-1}$, and (c) first excited state wave function $E = -7.837 \text{ cm}^{-1}$ (in $\text{\AA}^{-1/2}$) with respect to the dissociation limit.

D. Observables

By solving the set of coupled differential equations (9) on a radial grid R_k , all the observables of interest can be computed as a function of time. Note that all the operators are diagonal in M ; hence, one propagation is run for each M_0 value of a given initial J_0 value of J . The observables below are thus calculated for a given (J_0, M_0) value. They are then averaged over a Boltzmann distribution if temperature effects are considered.

The observable that is most commonly used to quantify the degree of alignment and its time evolution is the expectation value $\langle \cos^2 \theta \rangle$,

$$\begin{aligned} \langle \cos^2 \theta \rangle(t) &= \langle \Psi(t) | \cos^2 \theta | \Psi(t) \rangle \\ &= \sum_{R_k} \sum_{n'n} C_n^*(R_k, t) C_{n'}(R_k, t) \langle n | \cos^2 \theta | n' \rangle, \end{aligned} \quad (19)$$

where $\langle n | \cos^2 \theta | n' \rangle$ is given in Eq. (14).

The rotational excitation can be characterized by the expectation value of \mathbf{J}^2 as

$$\langle \mathbf{J}^2 \rangle(t) = \langle \Psi(t) | \mathbf{J}^2 | \Psi(t) \rangle = \sum_{R_k} \sum_n |C_n(R_k, t)|^2 J_n(J_n + 1) \quad (20)$$

as well as by the time evolution of the population of each J state, given by

$$P_J(t) = \sum_{R_k} \sum_{l\Omega} |C_{JM_0l\Omega}(R_k, t)|^2. \quad (21)$$

The angular distribution of the helium in the BF system is characterized by the probability density as a function of θ^{BF} ,

$$P(\theta^{BF}, t) = \sum_{R_k} \sum_{n'n} C_n^*(R_k, t) C_{n'}(R_k, t) \Theta_{n'}(\theta^{BF}) \Theta_n(\theta^{BF}). \quad (22)$$

Its time evolution is of particular interest: it is expected to remain unchanged if the He atom follows rigidly the rotation of CH_3I .

Information on the dynamics of the helium atom motion with respect to CH_3I is also given by the time evolution of the population of each l state,

$$P_l(t) = \sum_{R_k} \sum_{J\Omega} |C_{JM_0l\Omega}(R_k, t)|^2. \quad (23)$$

The temperature of helium nanodroplets in usual experimental conditions is 0.4 K; thus, the time evolution of the expectation value of $\langle \cos^2 \theta \rangle$ corresponds to the Boltzmann average of the observable $\langle \cos^2 \theta \rangle_{av}(t)$ for $T = 0.4$ K. It is obtained from the pure rotational state analogs $\langle \cos^2 \theta \rangle_{J_0 M_0}(t)$ for a given (J_0, M_0) value as

$$\langle \cos^2 \theta \rangle_{av}(t) = \sum_{J_0 M_0} w_{J_0 M_0}(T) \langle \cos^2 \theta \rangle_{J_0 M_0}(t) \quad (24)$$

with

$$w_{J_0 M_0}(T) = \exp(-E_{J_0 M_0}/kT) \left(\sum_{J_0' M_0'} \exp(-E_{J_0' M_0'}/kT) \right)^{-1}$$

The initial states considered in the Boltzmann average were obtained by imaginary time propagation (for $J_0 = 0$) or by diagonalization of H_{rot} (for $J_0 = 1$). In the latter case, H_{rot} is expressed in a basis of Wang states,⁴⁶ which are eigensolutions of \mathbf{J}^2 , J_Z , \mathbf{I}^2 , and the parity operator,

$$\begin{aligned} |n\epsilon\rangle &= |J_0 M_0 l \bar{\Omega} \epsilon\rangle \\ &= \frac{1}{\sqrt{2(1 + \delta_{\bar{\Omega}0})}} \left[|J_0 M_0 l \bar{\Omega}\rangle + \epsilon(-1)^{J_0} |J_0 M_0 l - \bar{\Omega}\rangle \right] \end{aligned} \quad (25)$$

with $\bar{\Omega} = |\Omega|$ and a DVR (discrete variable representation) representation⁴⁷ for the radial coordinate. The resulting energies (independent of M_0) are shown in Table I.

E. Dissociation

As strong laser intensities are employed, high rotational states can be excited. Therefore the rotational kinetic energy

TABLE I. Bound ground state energies of the $^4\text{He}-\text{CH}_3\text{I}$ complex for $J_0 = 0$ and 1 states.

	J	ϵ	Energy (cm^{-1})
Imaginary time	0	+1	-13.001
Diagonalization in the basis of Wang states	1	+1	-12.691
		-1	-12.525
		-1	-12.445

can become larger than the CH₃I binding energy and the complex can dissociate.

If the wave packet reaches the end of the grid, it must be absorbed to eliminate reflections at the boundaries which would interfere with the wave packet propagation.^{48,49} This absorption was implemented by multiplying the wave function at each time step by an exponentially decreasing function $f(R)$ between $R_{max} - \Delta$ and R_{max} ,

$$f(R) = \begin{cases} 1 & \text{for } R < R_{max} - \Delta \\ \exp\left[-\gamma\left(\frac{R - R_{max} - \Delta}{\Delta}\right)^2\right] & \text{for } R \geq R_{max} - \Delta \end{cases} \quad (26)$$

with $R_{max} = 53 \text{ \AA}$ and $\Delta = 12.4 \text{ \AA}$ which corresponds to 64 grid points. The absorption was optimized by trial and error, checking for reflections which can be observed as oscillations in the time evolution of the radial distribution of the wave packet at a long range. A value of $\gamma = 0.009$ leads to the complete elimination of reflections for the intensities studied in this work.

The radial probability distribution $P(R, t)$ at different times is shown in Fig. 3 after a strong laser pulse of $I_0 = 1.12 \times 10^{13} \text{ W/cm}^2$ and 450 fs duration. The pulse envelope is given by Eq. (4) with its maximum at half duration. Within 10 ps, a large amount of the wave packet has traveled around 50 Å and reached the grid boundary where it has been absorbed. This roughly corresponds to a speed of 500 m/s (5 Å/ps) and a kinetic energy of more than six times the binding energy. After 80 ps, a good part of the wave packet has dissociated, and a significant portion ($\approx 20\%$) remains trapped in the bound region $R \leq 10 \text{ \AA}$, not being able to dissociate. Hence we stop the propagation at $t = 80 \text{ ps}$.

F. Dissociative vs. bound part

It is important to note that the absorbed wave packet components contain information about the CH₃I molecule rotation

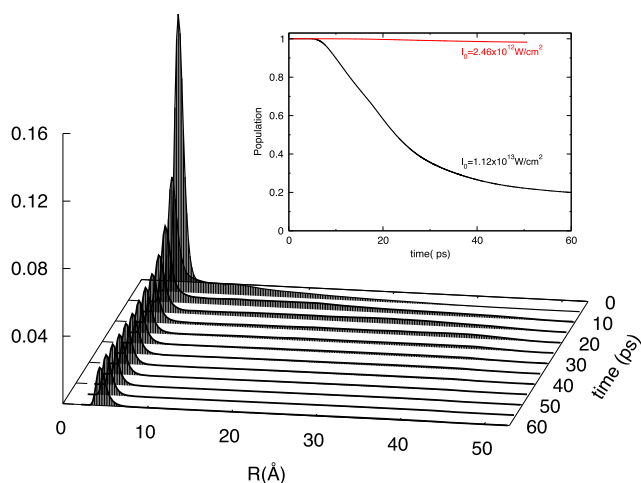


FIG. 3. Time evolution of the probability distribution for the distance between the He atom and the center of mass of the CH₃I molecule after a strong pulse of maximum intensity $1.12 \times 10^{13} \text{ W/cm}^2$ and 450 fs duration. By employing absorbing boundary conditions starting from $R_{max} - \Delta = 40.6 \text{ \AA}$, spurious reflections are eliminated. *Inset*: Time evolution of the norm of the wave function. For high intensities, after 60 ps, the norm stays constant at around 0.2, which corresponds to $\approx 20\%$ of the wave packet that remains trapped in the bound region.

and alignment. Hence, when dissociation occurs, the absorbed part of the wave packet also contributes to the $\langle \cos^2 \theta \rangle$ expectation value characterizing alignment and Eq. (19) can no longer be used. This information must be measured before the wave function is absorbed. Thus, the probability current at a defined distance R_I smaller than R_{max} is integrated over time as in Ref. 31. R_I should be chosen large enough that the interaction potential $V(R, \theta^{BF})$ is negligible compared to the CH₃I rotational constant for any angle θ^{BF} . Furthermore, the rotational energy $Bj(j+1)$ should be larger than the centrifugal potential $\hbar^2 l(l+1)/2\mu R_I^2$ for all possible combinations of j and l . These two conditions ensure that CH₃I can be considered as a free rotor for $R > R_I$. Finally, the laser pulse must be over before any component of the wave packet reaches $R = R_I$. These conditions are fulfilled for $R_I \approx 38 \text{ \AA}$.

Including this contribution, Eq. (19) needs to be completed by an asymptotic part which can be evaluated by a flux analysis across R_I . In practice, this analysis needs to be performed in a basis set of rotational eigenstates of the fragments,

$$\begin{aligned} \langle \cos^2 \theta \rangle(t) &= \langle \Psi(t) | \cos^2 \theta | \Psi(t) \rangle \\ &= \sum_{R_k < R_I} \sum_{m' m} A_{m'}^*(R_k, t) A_m(R_k, t) \langle m' | \cos^2 \theta | m \rangle \\ &\quad + \sum_{m' m} \langle m' | \cos^2 \theta | m \rangle U_{jj'}(t) \int_0^t dt' U_{jj}(t') I_m^{m'}(R_I), \end{aligned} \quad (27)$$

where $U_{jj'}(t') = e^{\frac{iB}{\hbar}[j(j+1) - j'(j'+1)]t'}$ is a phase factor and the probability current is given by

$$I_m^{m'}(R_I) = \frac{i\hbar}{2\mu} [A_{m'}(R_I) \nabla A_m^*(R_I) - A_m^*(R_I) \nabla A_{m'}(R_I)]_{R=R_I}. \quad (28)$$

Here, $|lm\rangle = |JjIM\rangle$ are basis functions in the coupled space-fixed (coupled SF) representation and A_m are the corresponding coefficients for the expansion of the wave packet. The transformation of the wave packet coefficients from the BF [Eq. (7)] to the coupled SF basis functions can be obtained by

$$A_m(R, t) = \sqrt{2j+1} (-1)^J \sum_{\Omega} (-1)^{\Omega} \begin{pmatrix} l & j & J \\ \Omega & 0 & -\Omega \end{pmatrix} C_n(R, t). \quad (29)$$

The first term in Eq. (27) corresponds to the inner part of the wave packet ($R \leq R_I$) which at longer times ($t > 60 \text{ ps}$) is the part that remains bound. It can also be calculated in the BF basis as in Eq. (19). The second term corresponds to the dissociative part of the wave packet.

For an isolated molecule, $e^{-iBj(j+1)(t-t')/\hbar}$ results from applying the time evolution operator to a $|jM_j\rangle$ stationary state. The time evolution of the expectation value for the dissociated fraction of the wave packet is included in the phase factor $U_{jj'}(t)$. This time evolution corresponds to that of a freely rotating molecule, when the molecule and the helium are no longer interacting.

G. Numerical specifications

For the numerical calculations, the basis set for the propagation must be very large since the laser pulses studied in this

work can excite the $^4\text{He}-\text{CH}_3\text{I}$ complex to states with J higher than 30 (and $j > 50$) and produce very fast initial dissociation. Based on convergence tests, the basis set includes all the functions $|JMI\Omega\rangle$ [Eq. (8)] or $|JjIM\rangle$ [introduced in Eq. (28)] with $J \leq 35$, $l \leq 20$, $|\Omega| \leq 20$, and $j \leq 55$.

Note that all operators are diagonal in M , but the matrix elements for both the laser-system interaction [Eqs. (13) and (14)] and the potential [Eq. (18)] depend on M . Hence for a given initial J_0 value, one simulation is run for each M_0 value. The simulations are conducted for initial rotational states $(J_0, M_0) = (0, 0), (1, 0), (1, \pm 1)$.

The grid in R extends from $R_{\min} = 2.17 \text{ \AA}$ to $R_{\max} = 53 \text{ \AA}$ with 256 grid points, resulting in a grid spacing of $\Delta R = 0.198 \text{ \AA}$. The propagation time is 80 ps with a time step of 5 fs. The time evolution of the wave packet during and after the pump laser pulse is determined by solving the time dependent Schrödinger equation with the Crank-Nicholson method.⁵⁰

III. RESULTS

In this section, we present and discuss the results obtained from the numerical simulation of the time evolution of the $^4\text{He}-\text{CH}_3\text{I}$ complex after the application of a laser pulse to induce molecular alignment. In particular, we determine different observables in order to understand the mechanism behind the non-adiabatic alignment of molecules weakly interacting with an environment in conditions similar to helium nanodroplet experiments ($T = 0.4 \text{ K}$).

A. Molecular alignment: High vs. low intensities

The alignment dynamics, characterized by $\langle \cos^2 \theta \rangle$, is shown in Fig. 4. There one can observe the effect of the laser pulse intensity and of the temperature on the degree of alignment of the $\text{He}-\text{CH}_3\text{I}$ complex compared to that of the free CH_3I molecule. The pulse parameters are similar to the

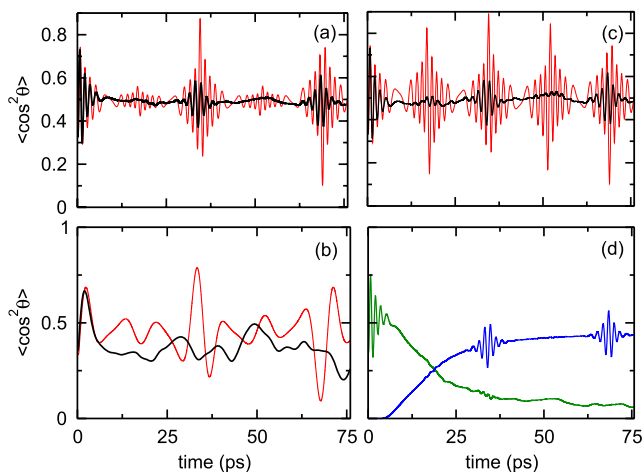


FIG. 4. Alignment dynamics of the $^4\text{He}-\text{CH}_3\text{I}$ complex represented by $\langle \cos^2 \theta \rangle$ as a function of time. [(a)–(c)] Comparison of the $^4\text{He}-\text{CH}_3\text{I}$ alignment (black) with free CH_3I alignment (red), for a laser pulse intensity [Eq. (4)] and temperature of (a) $I_0 = 1.12 \times 10^{13} \text{ W/cm}^2$ and $T = 0.4 \text{ K}$, (b) $I_0 = 2.46 \times 10^{12} \text{ W/cm}^2$ and $T = 0.4 \text{ K}$, (c) $I_0 = 1.12 \times 10^{13} \text{ W/cm}^2$ and $T = 0 \text{ K}$. (d) Alignment dynamics of the bound part (green) and the dissociative part (blue) of the wave packet for $I_0 = 1.12 \times 10^{13} \text{ W/cm}^2$ and $T = 0.4 \text{ K}$.

experimental ones used to induce non-adiabatic alignment of isolated molecules in the gas phase. The intensity of the alignment pulse [$I = 1.12 \times 10^{13} \text{ W/cm}^2$ for plots (a), (c), and (d) in Fig. 4] was selected such that the expectation value $\langle J^2 \rangle \approx 400$, which leads to gas phase alignment for a laser pulse of $\tau = 450 \text{ fs}$ duration.^{26,32} We also show for comparison the results for an intensity 4.5 times smaller in Fig. 4, plot (b), corresponding to $\langle J^2 \rangle \approx 16$ (see Fig. 5).

Figure 4(a) shows the calculated $\langle \cos^2 \theta \rangle$ as a function of time for isolated CH_3I molecules (red) and for the $^4\text{He}-\text{CH}_3\text{I}$ complex (black) for an alignment laser pulse of $I_0 = 1.12 \times 10^{13} \text{ W/cm}^2$ intensity and $\tau = 450 \text{ fs}$ duration, and a temperature of 0.4 K , characteristic of He nanodroplets. At this temperature, the Boltzmann average of the signal only includes $J = 0$ and $J = 1$ rotational states, higher J -states contributing less than 5% to the thermal population. In the case of the isolated molecule, the structure exhibits a prompt alignment peak shortly after the pulse and prominent transients repeating periodically in time ($\tau_{\text{rot}} = 66.6 \text{ ps}$), in agreement with the results of previous studies on the calculation of the non-adiabatic alignment of the CH_3I molecule.²⁶ For the complex, the $\langle \cos^2 \theta \rangle$ curve resembles that of the isolated molecule. The initial prompt peak is identical, and the narrow transients appear at the same time intervals although the amplitudes are significantly smaller.

For $T = 0 \text{ K}$, that is, when considering only the contribution of $J = 0$ in the calculation of $\langle \cos^2 \theta \rangle$ [Fig. 4(c)], the alignment dynamics barely changes from the results at $T = 0.4 \text{ K}$. The only noticeable difference is the quarter revival at $t \approx 17 \text{ ps}$ in the case of $T = 0 \text{ K}$, which almost disappears when the $J = 1$ state is included at $T = 0.4 \text{ K}$, for both the isolated molecule and the complex.

An important aspect to consider for high intensities is the dissociation probability. As already discussed in Sec. II E, the complex rapidly starts dissociating for $t \geq 7 \text{ ps}$, and after 60 ps the norm, which corresponds to the part of the wave packet that remains bound, stabilizes around 0.2. The dissociation probability and its effect on the rotational revivals will be discussed in more detail below.

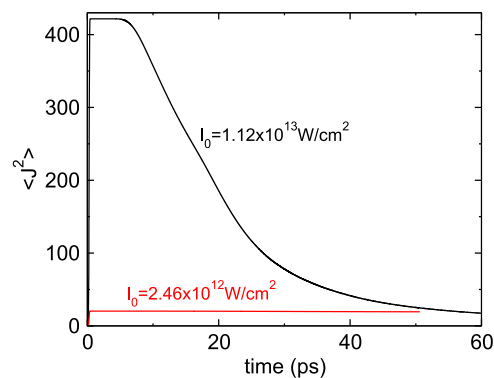


FIG. 5. Time evolution of the expectation value of J^2 of the $^4\text{He}-\text{CH}_3\text{I}$ complex for two different laser intensities. For the higher intensity, $I_0 = 1.12 \times 10^{13} \text{ W/cm}^2$, the expectation value of J^2 rises to ≈ 400 , meaning that a distribution of J states around 20 are initially populated. After the dissociation of the complex, this value decays to $\langle J^2 \rangle \approx 16$ corresponding to a distribution of J states around 5. $\langle J^2 \rangle \approx 16$ is also the maximum value obtained after the pulse with the lower intensity, $I_0 = 2.46 \times 10^{12} \text{ W/cm}^2$, where the complex does not dissociate.

Dissociation can be avoided by lowering the intensity of the alignment pulse. For $I_0 = 2.46 \times 10^{12}$ W/cm² and $\tau = 450$ fs, the norm barely decays (see the inset of Fig. 3), so the pulse is not powerful enough to dissociate the complex. Under these conditions, the calculation of $\langle \cos^2 \theta \rangle(t)$ reveals an alignment dynamics in Fig. 4(b) which differs from the one for higher intensities [Fig. 4(c)]. The rise time of the first alignment peak is longer, and it is followed by a broad revival structure for isolated CH₃I (red), and by slow oscillations with no significant sign of revivals in the case of ⁴He-CH₃I (black). For gas phase CH₃I, the transients occur at the same time intervals as for higher intensity because all energy levels are multiples of the same rotational constant. The change from typical sharp transient recurrences to broad structures as the intensity is lowered corresponds to the smaller number of J -states coherently populated by the lower intensity laser pulse.

Note that the ⁴He-CH₃I complex is not linear, so the time intervals at which the rotational components of the wave packet rephase no longer depend on one single rotational constant. Thus, the position of rotational revivals, if they existed, should be different from those of the isolated CH₃I molecule. In an attempt to assign the broad structures observed for He-CH₃I in Fig. 4(b) to possible half revivals, we have estimated the rotational periods of the complex from its rotational constants deduced from the energy difference between the $J = 0$ and 1 rotational energy levels (see Table II). The results were not conclusive. Hence we do not expect revivals to appear at larger times. Note that the ⁴He-CH₃I complex is very flexible; hence, the rotational “constants” are only an approximation to a rigid top. A piece of evidence of this is that since the complex is modeled as a triatomic, it should be planar; hence, the following relationship should hold: $\frac{1}{C_p} = \frac{1}{A} + \frac{1}{B}$.³⁴ This is the second value (C_p) in Table II. The two values for the C constant differ by $\sim 10\%$.

We now turn to examine the dissociation process and the role it plays in the alignment signal. We first examine separately the alignment dynamics corresponding to the bound and the dissociating fractions of the wave packet [first and second terms in Eq. (27)] in Fig. 4(d) for the same laser parameters as in Fig. 4(a). For the bound fraction, the initial prompt alignment remains unchanged, but the following defined transient revivals disappear. Hence the helium atom is clearly changing the rotational dynamics of the complex with respect to that of the isolated molecule. The half and the first revivals at $t \approx 33$ ps and $t \approx 66$ ps, respectively, observed in Fig. 4(a), are due to the dissociative part of the wave packet [Fig. 4(d)], which explains why they occur at the same times as for the

bare CH₃I molecule. The initial prompt alignment signal is unaffected because these oscillations come from coherent population of high J levels, with no rotation involved. Therefore their period roughly corresponds to $h/(\Delta E)$, with $\Delta E = B(4\langle J \rangle + 6)$ being the energy difference between two rotational levels $\langle J \rangle$ and $\langle J + 2 \rangle$ with $\langle J \rangle = 20$ (the laser-system interaction operator couples J with $J \pm 2$ for $M = 0$).

B. Rotational analysis

1. Rotational distribution

In order to get more insight into the alignment and dissociation processes, we calculated the time evolution of different observables related to the rotation of the molecule and of the complex. Only the dynamics starting from the initial wave function with $J = 0$ is considered in the following since the $T = 0$ K alignment dynamics does not significantly differ from the $T = 0.4$ K Boltzmann averaged one.

The efficiency of molecular alignment depends on the degree of rotational excitation, that is, the number of rotational J -states excited by the laser pulse. Figure 6 shows the population of J -states in the renormalized bound fraction of the wave packet, i.e., the wave packet divided by its norm, which can differ from 1 because of absorption, in order to show the relative J population for the part remaining in the simulation grid. The expectation value of J^2 was already shown in Fig. 5. At the end of the higher intensity (1.12×10^{13} W/cm²) laser pulse, the population is found to be distributed among many

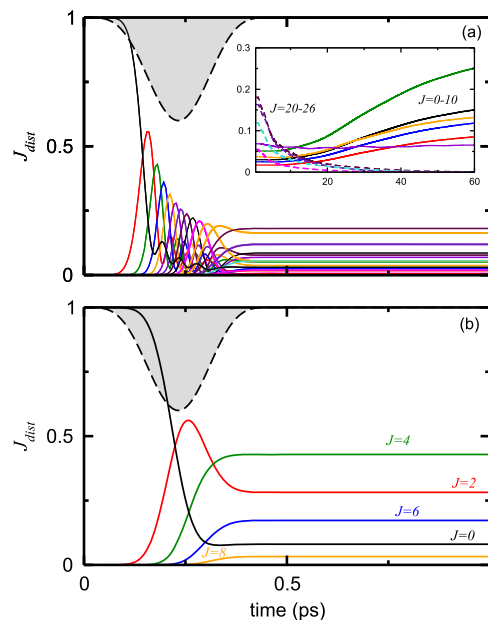


FIG. 6. Time evolution of the ⁴He-CH₃I J rotational distribution calculated from Eq. (21) and renormalized (see text for details), for (a) $I_0 = 1.12 \times 10^{13}$ W/cm² and (b) $I_0 = 2.46 \times 10^{12}$ W/cm². The laser pulse is visualized in negative, attached to the upper abscissa axis (dashed line with the grey shaded area). In (a), high rotational states up to $J = 26$ are initially populated. At later times (inset), the highest J -components are carried away by the dissociating part of the wave packet, leading to the loss of the initial strong alignment and the absence of revivals for the bound complex. At lower intensities (b), fewer and lower J -states (up to $J = 10$) are populated. Note that only even J 's are populated because initially $J = 0$ which implies $M = 0$ at all times: it is a property of the 3- j symbols in Eq. (14) that the sum of the angular momenta in the first row be even when the second row has only zeros.³⁴

TABLE II. Rotational constants (cm⁻¹) and corresponding rotational periods (ps) of the ⁴He-CH₃I complex approximated by a rigid top (see text), left columns, and of CH₃I (right column).

	He-CH ₃ I				CH ₃ I
	A	B	C	C_p	B
cm ⁻¹	0.361	0.194	0.115	0.126	0.250
ps	46.15	85.63	145.08	131.78	66.6

rotational states up to $J = 26$, corresponding to a strong alignment in Fig. 4. The population of each rotational state remains constant up to ~ 7 ps. At larger times, when the complex starts dissociating, higher J -states decrease to zero as shown in the inset of Fig. 6(a), therefore increasing the relative population of lower rotational states, until only $J \leq 10$ states remain. This is consistent with the interpretation that high rotational states dissociate and that the transients observed at $t \approx 33$ and $t \approx 66$ ps in Fig. 4(a) or 4(c) are due to the alignment of a CH₃I molecule dissociated from the He atom and corresponding to high rotational excitation. Also, the disappearance of the revival pattern for the bound part of the complex in Fig. 4(d) is due at least partly to the loss of high rotational levels.

For the lower intensity (2.46×10^{12} W/cm²) alignment pulse, fewer and lower J -states are populated as can be seen in Fig. 6(b). In this case, the rotational wave packet is composed of the $J = 0$ to $J = 8$ states and leads to the broader and non-regular alignment structure observed in Fig. 4(b).

2. Angular distribution in the BF frame: l distribution

To gain further insight into the alignment of molecules weakly interacting with He, we study the dynamics of the angular distribution in the BF (rotating frame) representation.

The time evolution of the l -states population is presented in Fig. 7. The initial ground state bending function is mainly composed of $l = 0$ to $l = 5$ states. For the lower intensity kick pulse presented in Fig. 7(b), the l state population remains mostly in the $l = 0$ –5 manifold, meaning that the helium atom and the CH₃I molecule rotate together as a whole. On the

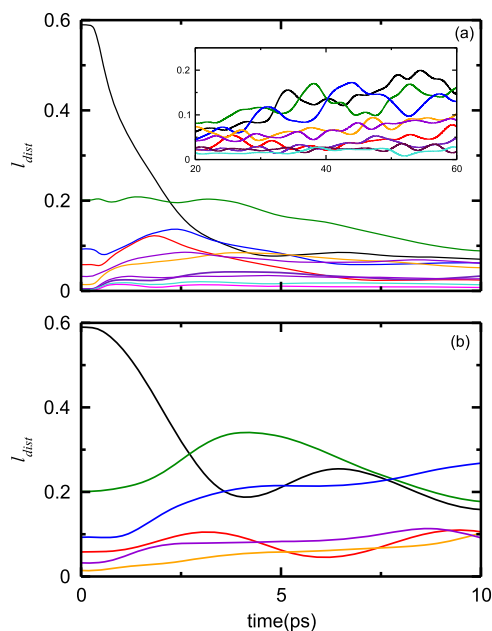


FIG. 7. Time evolution of the population of l -states after the interaction of the ⁴He–CH₃I system with a laser pulse of (a) $I_0 = 1.12 \times 10^{13}$ W/cm² and (b) $I_0 = 2.46 \times 10^{12}$ W/cm². For the higher intensity, the population is distributed among many different orbital angular states that mix during the dynamics. On the other hand, for the lower intensity, the initial l -state population remains mostly in the $l = 0$ –5 manifold. This means that the complex rotates as a whole, that is, the He atom follows the rotation of CH₃I.

contrary, for the higher intensity presented in Fig. 7(a), higher l states are populated and mix after the laser is turned off. This shows that the He rotation is excited in the frame rotating with CH₃I. In other words, it is not able to follow the fast rotation of the molecule.

3. Angular distribution in the BF frame: θ^{BF} distribution

The angular motion of the He atom relative to that of CH₃I can be observed directly by looking at Fig. 8, which displays the time evolution of the probability density as a function of the angle θ^{BF} between the He atom and the C–I axis of the molecule [Eq. (22)]. Initially, the density is localized around $\theta^{BF} = 0.61\pi$ (1.91 rad or 109°), which corresponds to the ground state geometry of the complex.

For a pulse with peak intensity $I_0 = 1.12 \times 10^{13}$ W/cm², the probability density shown in Fig. 8(a) decreases due to dissociation, as already noted in Secs. II E and III A. However, it first begins to oscillate between $\theta^{BF} = 0$ and $\theta^{BF} = \pi$ in less than 5 ps. This is not surprising since the first excited van der Waals level is only about 5 cm^{−1} above the ground level, and it corresponds to quasi-free rotation around CH₃I as can be seen in Fig. 2(c). Hence most of the wave packet corresponds to He rotating faster and faster around CH₃I in the BF frame (CH₃I rotating faster and faster in the SF frame and “losing” the He atom), before acquiring enough energy to dissociate. The low anisotropy of the interaction potential makes it possible for the He atom to rotate around the molecule with almost no collision, hence maintaining the coherence of the angular wave

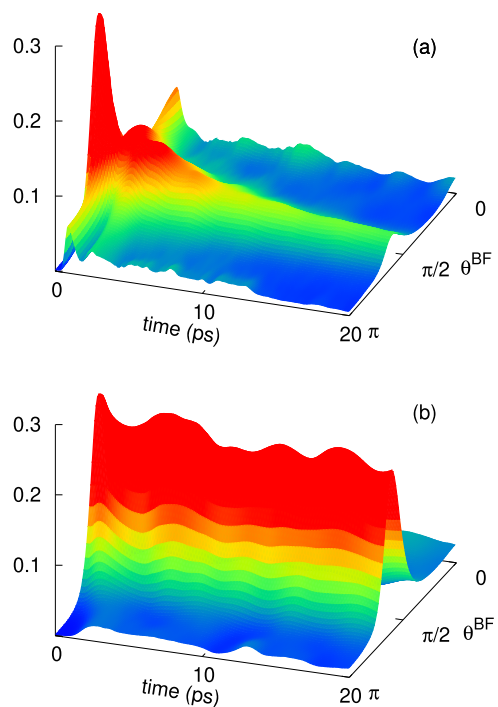


FIG. 8. Time evolution of the probability density in θ^{BF} describing the angular distribution of the helium atom in the body-fixed system. (a) For a laser pulse with $I_0 = 1.12 \times 10^{13}$ W/cm², the probability density rapidly spreads between $\theta = 0$ and $\theta = \pi$, that is, the He atom is not able to follow the fast rotation of the CH₃I molecule. (b) For a laser pulse with $I_0 = 2.46 \times 10^{12}$ W/cm², the probability density remains always localized around the initial θ angle, which corresponds to the configuration of the ground state of the complex. In this case, the He atom rotates together with the molecule.

packet, which explains the revivals observed after dissociation. After about 40 ps, the probability density settles again around the initial angle. This is consistent with the duration of the dissociation process of the complex (see Fig. 3): the remaining bound part of the wave packet relocalizes around the minimum of the interaction well; hence, the He atom follows the rotation of the CH₃I molecule.

By contrast, if the intensity is set to 2.46×10^{12} W/cm², the probability density evolves always localized at the initial θ^{BF} angle as can be seen in Fig. 8(b). In this case, the helium atom can follow the rotation of the molecule. This gives rise to a radically different alignment dynamics than for the strong pulse as shown in Fig. 4.

In order to gain a more detailed view of the rotational excitation and subsequent dissociation process for the higher intensity case, we analyze in Fig. 9 the probability distribution $P(R, \theta^{BF})$ defined by $P(R, \theta^{BF}) = \sum_{n'n} C_n^*(R_k, t) C_{n'}(R_k, t) \Theta_{n'}(\theta^{BF}) \Theta_n(\theta^{BF})$, as a function of time. The upper left panel of Fig. 9 [$t = 0$ ps, (a)] shows the initial bound wave function, with a maximum at 4.24 Å and $\theta = 0.61\pi$ (1.91 rad or 109°) (the difference with the distance at the potential minimum, $R_e = 3.97$ Å, is due to anharmonicity and zero-point delocalization). At the end of the laser pulse [$t = 0.5$ ps, (b)], a large part of the distribution is delocalized in the θ^{BF} direction, without any significant displacement in the R direction. This means that the rotational excitation of the ⁴He-CH₃I initially leads to an angular excitation of the helium atom in the BF frame, i.e., He is not able to follow

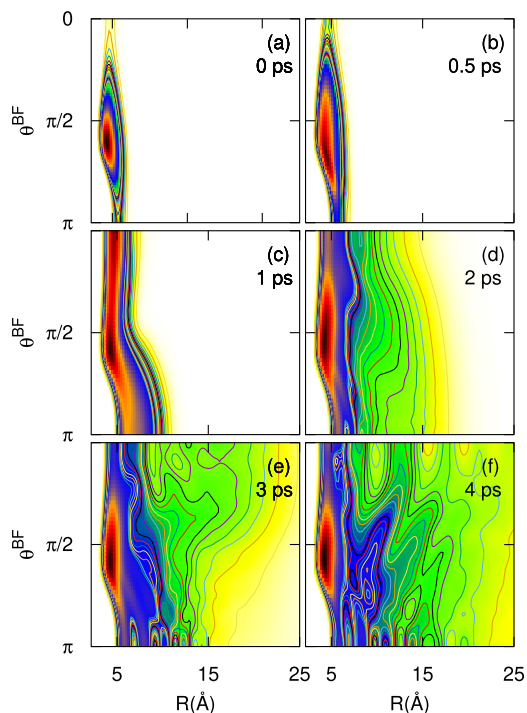


FIG. 9. Snapshots of the probability distribution $P(R, \theta^{BF})$ as a function of the He-CH₃I distance R and angle θ^{BF} , at $t = 0$ (switch on of the laser pulse), 0.5 ps (switch off of the laser pulse), and 1, 2, 3, and 4 ps (laser free dynamics). Comparing with the initial, bound wave function at $t = 0$ ps (a), the distribution first spreads in the θ^{BF} direction during and after the laser pulse [(b) and (c)], corresponding to an angular excitation of the helium atom in the BF frame. At later times [(d)–(f)], the wave packet spreads in R , i.e., moves to larger distances, resulting in the dissociation of the complex.

the rotation of CH₃I. Only at later times [$t = 1$ ps, (c)] does the wave packet start moving to larger R -distances, indicating the onset of the dissociation process. Interestingly, this extension toward large distances takes preferentially place at angles around $\theta^{BF} \approx \pi$, i.e., at the CH₃ side. This changes at later times [$t = 2$ and $t = 3$ ps, (c) and (d)], where the helium atom moves further away from the complex on the iodine side. Finally, for $t = 4$ ps (e) onwards, the wave packet corresponding to the dissociation shows a structured but nearly isotropic distribution in θ^{BF} , meaning that the dissociation has no preferential angular distribution. The looser structure on the iodine side reflects the fact that the interaction potential is going to zero more slowly at long distances than on the carbon side.

Hence the dissociation proceeds via a strong rotational excitation, and there is no clear sign of the CH₃I molecule kicking the He atom when it starts rotating so fast that the atom cannot follow.

IV. CONCLUSIONS

We have modeled the non-adiabatic laser alignment of a van der Waals complex formed with the CH₃I molecule and a helium atom using a rigid diatomic approximation of the CH₃I rotor. All the other degrees of freedom (CH₃I rotation, He bound or dissociated motion) were described using a quantum mechanical wave packet propagated on a model potential energy surface for the molecule-atom interaction. This way, we could directly model the alignment signal, as a first step in view of comparing with the experiments presented in Ref. 26.

From the results, it is clear that the alignment dynamics strongly depends on the intensity of the initial laser pulse. We show that high intensities are needed for an efficient alignment, which, however, leads to the dissociation of the complex. A strong pulse populates high rotational energy levels, making the molecule rotate fast. For 80% of the wave packet, the rotational energy exceeds the binding energy of the complex, resulting in the ejection of the helium atom. The proportion of the wave packet that dissociates depends on the laser pulse intensity since with the lower intensity used in this work we observe almost no dissociation. On the other hand, Søndergaard *et al.*³¹ have found that He-CS₂ or He-HCCH does not reach 100% dissociation when further increasing the intensity. We have not attempted to check if a limit lower than 100% also existed for He-CH₃I at higher intensities.

In this higher intensity regime, the degree of alignment is obtained by adding the signal calculated from the dissociated components of the wave packet to the signal corresponding to the bound part. The alignment dynamics resembles that of isolated CH₃I, with revivals at the same time intervals due to the dissociated part. On the other hand, when lower intensities are used, the pulse is not powerful enough to populate high rotational states. As a result, there is an initial alignment peak, but the subsequent signal is broad and does not show any clearly assignable structure. In addition, the helium atom remains attached and keeps interacting with the CH₃I molecule. The same behavior is observed for the bound part

of the wave packet remaining after dissociation when a strong pulse is applied. The interaction of the helium atom with the molecule affects its rotation and leads to the disappearance of the revivals. Instead, broad and slow oscillations are observed, resembling the $\langle \cos^2 \theta \rangle$ structure for low laser intensities. As noted by Galinis *et al.*¹⁹ in their study of the acetylene-helium complex, these oscillations are due to rotational as well as van der Waals excited states.

The experiments on laser induced alignment of CH₃I solvated in helium nanodroplets by Pentlechner *et al.*²⁶ revealed initial alignment but, unlike our results, with a dynamics that is much slower than in the gas phase and no sign of revivals. In addition, it was found that the maximum degree of alignment for this initial peak gradually occurred at later times and decreased as the intensity was lowered. In a more recent publication on I₂ in helium nanodroplets, Shepperson *et al.*²⁹ also observed initial alignment with a width that depended on the kick pulse intensity. In addition, at low intensities (1.2 J/cm²), the prompt alignment peak was followed by oscillations decaying out at larger times. At very large fluences, this structure disappeared. Using the angulon quasiparticle theory,³⁰ they interpreted the structure observed at low intensities as a manifestation of coherent rotation of the molecule and its local helium solvation shell. At high intensities, they proposed that several He atoms detach from the I₂ molecule, leaving it almost freely rotating inside a bubble.

Extrapolating our results to a helium droplet environment, both the low and the high intensity regimes do lead to an initial prompt alignment peak, with a structure similar to that of the free molecule at the same intensity. The low intensity regime could lead to an oscillatory structure after that, but with no clear recurrence, and the structure would require a frequency analysis to assign it.¹⁹ In the high intensity regime, our results show that the 80% of the wave packet corresponding to freely rotating CH₃I should exhibit the same recurrences as the free molecule. Of course, the dissociating helium atoms would not necessarily leave the droplet because of the surrounding helium, but, as suggested by Shepperson *et al.*,²⁹ the molecule would end up rotating freely inside a “bubble.” However, this signal would be superimposed to that of the ~20% of the wave packet which remains bound and exhibit no revival structure after the initial alignment. The disappearance of the recurrences in the droplet could be due to the fact that the molecule is initially surrounded by a large number of atoms so that a number of them could remain bound inside the bubble mentioned above. Hence the contribution of the part of the wave packet that remains bound could win over the freely rotating part.

Our results on the ⁴He-CH₃I complex presented in this work can also be compared to the theoretical study of Søndergaard *et al.*³¹ on the nonadiabatic alignment dynamics of the acetylene and of the CS₂ molecule complexed to a He atom. When one aims at comparing to an experimentally measured signal, an average over the spatial laser beam profile should be performed, as has been done in their work. Comparing with our results, one finds a similar qualitative behavior of the alignment dynamics. Since in our case we focus on the study of the alignment dynamics itself as a function of laser intensity, we do not average over intensities. For high

intensity of the initial kick pulse, a similar alignment signal $\langle \cos^2 \theta \rangle$ was obtained for CS₂ and its van der Waals complex with He. This was attributed to fast dissociation of the complex, as we observe in this work on ⁴He-CH₃I. The small difference in the permanent alignment level between recurrences at long times was attributed to the loss of angular momentum taken away by the departing He atom. In our case, the most notable difference between CH₃I and He-CH₃I is the lower intensity of the recurrences, which we attribute to the 20% of the wave packet which remains trapped in the van der Waals well. For a lower intensity kick pulse, Søndergaard *et al.* obtained the same prompt alignment peak as for free CS₂, which is also true in this work for CH₃I. However, revival peaks were still present, albeit less pronounced, slightly broader and appearing later than for the isolated molecule, whereas we obtain a broadly oscillating structure which shows no clear correspondence with the revivals observed for free CH₃I. We believe that this difference in behavior is due to the larger masses and deeper ($D_e = 54 \text{ cm}^{-1}$)⁵¹ and more anisotropic well involved for CS₂, which makes the complex behave more like a quasi-rigid molecule. The case of the acetylene-He complex was more involved,³¹ with a prompt alignment peak unchanged as in the other cases but also a decay of the revivals for the complex at high intensity, which disappear after one rotational period. This is presumably due to the lower moments of inertia, as proposed by the authors. We think that the fact that the complex equilibrium configuration is linear with a large amplitude motion around that reference structure¹⁹ is also contributing to the loss of coherence. In that respect, He-CS₂ was more directly comparable to the case of He-CH₃I studied here since the bound state structure was perpendicular.

Our interpretation is based on the study of different observables related to the rotational dynamics of the system. In particular, the (R, θ^{BF}) probability distribution snapshots show that dissociation at high intensity proceeds via high rotational excitation of He in the frame rotating with the CH₃I molecule rather than colliding with it. We show that lower intensities prevent dissociation because they populate only low lying J -states, but this prevents efficient alignment and there is no clear recurrence. Angular distributions reveal that the molecule and the helium atom rotate as a whole in this case since the l -state population does not evolve much in time and the angle of the He atom with respect to the molecular C-I axis remains mainly constant. This is in agreement with the interpretation of the iodine molecule rotating together with the solvation shell in the nanodroplet experiment. On the other hand, we show that high intensities populate higher rotational states, which leads to an alignment signal resembling that of freely rotating molecules but leads to dissociation of the complex. Angular distributions show an important mixing of angular l -states and a strong variation of the He-molecule angle distribution, which confirm this mechanism where the helium atom is not able to follow the fast rotation and detaches from the molecule.

In conclusion, we have shown that initial alignment is induced by a laser pulse for molecules weakly interacting with a helium atom. The fate of this alignment at larger times when the laser is off depends on the intensity of the pulse. For

large intensities, recurrences can be observed when the initial pulse is sufficiently intense to populate high J states and dissociate the complex. The proportion of the wave packet remaining bound obviously depends on the well depth of the van der Waals interaction and on the energy of the rotational excitation achieved by the laser pulse. For lower intensities, the complex remains bound. Recurrences can be observed if the complex is rigid enough, although they are more involved than in the simple diatomic case because the complex will generally correspond to an asymmetric top. In the case of a collinear complex, the amplitude of the He angular motion is usually wide, which complicates the analysis. Extrapolating to helium nanodroplets, the high intensity case could produce a bubble around the rapidly rotating molecule if the intensity was high enough and the potential well shallow enough to ensure total dissociation. In this case, it would be expected to recover the sequence of recurrences of the free molecule. If dissociation is not complete because the well depth is deep, the broad and slowly oscillating signal from the complex composed of the molecule and the remaining bound atoms can hide the recurrences. The low intensity case is expected to produce a more or less complex alignment signal corresponding to the molecule and the helium atoms in direct interaction with it rotating as a whole. Further insight can be achieved by modeling molecular alignment inside superfluid helium droplets within the framework of density functional theory.⁵²

ACKNOWLEDGMENTS

M.B. thanks the Université Fédérale Toulouse Midi-Pyrénées for financial support through the “Chaires d’Attractivité 2014” Programme IMDYNHE. High performance computing resources from CALMIP (Grant No. P1039) are gratefully acknowledged. This work has been performed under Grant No. FIS2017-87801-P from (AEI/FEDER, UE, Spain).

¹H. Stapelfeldt and T. Seideman, *Rev. Mod. Phys.* **75**, 543 (2003).

²A. Rouzée, S. Guérin, O. Faucher, and B. Lavorel, *Phys. Rev. A* **77**, 043412 (2008).

³C. Horn, M. Wollenhaupt, M. Krug, T. Baumert, R. de Nalda, and L. Bañares, *Phys. Rev. A* **73**, 031401 (2006).

⁴C. Z. Bisgaard, O. J. Clarkin, G. Wu, A. M. D. Lee, O. Geßner, C. C. Hayden, and A. Stolow, *Science* **323**, 1464 (2009).

⁵M. G. Pullen, B. Wolter, A.-T. Le, M. Baudisch, M. Hemmer, A. Senftleben, C. D. Schröter, J. Ullrich, R. Moshhammer, C. D. Lin, and J. Biegert, *Nat. Commun.* **6**, 7262 (2015).

⁶I. V. Litvinyuk, K. F. Lee, P. W. Dooley, D. M. Rayner, D. M. Villeneuve, and P. B. Corkum, *Phys. Rev. Lett.* **90**, 233003 (2003).

⁷J. P. Cryan, P. H. Bucksbaum, and R. N. Coffee, *Phys. Rev. A* **80**, 063412 (2009).

⁸T. Seideman and E. Hamilton, “Nonadiabatic alignment by intense pulses. Concepts, theory, and directions,” in *Advances in Atomic, Molecular, and Optical Physics* (Academic Press, 2005), Vol. 52, pp. 289–329.

⁹T. Seideman, *Phys. Rev. Lett.* **83**, 4971 (1999).

¹⁰T. Seideman, *J. Chem. Phys.* **103**, 7887 (1995).

¹¹R. Robinett, *Phys. Rep.* **392**, 1 (2004).

¹²F. Rosca-Pruna and M. J. J. Vrakking, *Phys. Rev. Lett.* **87**, 153902 (2001).

¹³T. Seideman, *J. Chem. Phys.* **115**, 5965 (2001).

¹⁴H. Shima and T. Nakayama, *Phys. Rev. A* **70**, 013401 (2004).

¹⁵S. Ramakrishna and T. Seideman, *Phys. Rev. Lett.* **95**, 113001 (2005).

¹⁶J. Ohkubo, T. Kato, H. Kono, and Y. Fujimura, *J. Chem. Phys.* **120**, 9123 (2004).

¹⁷S. Minemoto and H. Sakai, *J. Chem. Phys.* **134**, 214305 (2011).

¹⁸J. Wu, A. Vredenburg, B. Ulrich, L. P. H. Schmidt, M. Meckel, S. Voss, H. Sann, H. Kim, T. Jahnke, and R. Dörner, *Phys. Rev. A* **83**, 061403 (2011).

¹⁹G. Galinis, C. Cacho, R. T. Chapman, A. M. Ellis, M. Lewerenz, L. G. Mendoza Luna, R. S. Minns, M. Mladenović, A. Rouzée, E. Springate, I. C. E. Turcu, M. J. Watkins, and K. von Haeften, *Phys. Rev. Lett.* **113**, 043004 (2014).

²⁰G. Galinis, L. G. Mendoza Luna, M. J. Watkins, A. M. Ellis, R. S. Minns, M. Mladenović, M. Lewerenz, R. T. Chapman, I. C. E. Turcu, C. Cacho, E. Springate, L. Kazak, S. Göde, R. Irsig, S. Skruszewicz, J. Tiggesbäumker, K.-H. Meiwes-Broer, A. Rouzee, J. G. Underwood, M. Siano, and K. von Haeften, *Faraday Discuss.* **171**, 195 (2014).

²¹J. M. Hartmann and C. Boulet, *J. Chem. Phys.* **136**, 184302 (2012).

²²J. P. Toennies and A. F. Vilesov, *Angew. Chem., Int. Ed.* **43**, 2622 (2004).

²³S. Grebenev, J. P. Toennies, and A. F. Vilesov, *Science* **279**, 2083 (1998).

²⁴R. Lehnig, P. L. Raston, and W. Jäger, *Faraday Discuss.* **142**, 297 (2009).

²⁵R. E. Zillich and K. B. Whaley, *Phys. Rev. B* **69**, 104517 (2004).

²⁶D. Pentlehner, J. H. Nielsen, A. Slenczka, K. Mølmer, and H. Stapelfeldt, *Phys. Rev. Lett.* **110**, 093002 (2013).

²⁷L. Christiansen, J. H. Nielsen, D. Pentlehner, J. G. Underwood, and H. Stapelfeldt, *Phys. Rev. A* **92**, 053415 (2015).

²⁸D. Pentlehner, J. H. Nielsen, L. Christiansen, A. Slenczka, and H. Stapelfeldt, *Phys. Rev. A* **87**, 063401 (2013).

²⁹B. Shepperson, A. A. Søndergaard, L. Christiansen, J. Kaczmarczyk, R. E. Zillich, M. Lemeshko, and H. Stapelfeldt, *Phys. Rev. Lett.* **118**, 203203 (2017).

³⁰M. Lemeshko, *Phys. Rev. Lett.* **118**, 095301 (2017).

³¹A. A. Søndergaard, R. E. Zillich, and H. Stapelfeldt, *J. Chem. Phys.* **147**, 074304 (2017).

³²E. Hamilton, T. Seideman, T. Ejdrup, M. D. Poulsen, C. Z. Bisgaard, S. S. Viftrup, and H. Stapelfeldt, *Phys. Rev. A* **72**, 043402 (2005).

³³G. Włodarczyk, D. Boucher, R. Bocquet, and J. Demaison, *J. Mol. Spectrosc.* **124**, 53 (1987).

³⁴R. Zare, *Angular Momentum* (Wiley, New York, 1988).

³⁵H.-J. Werner, P. J. Knowles, R. Lindh, F. R. Manby *et al.*, MOLPRO, version 2015.1, a package of *ab initio* programs, 2015, see <http://www.molpro.net>.

³⁶K. A. Peterson, *J. Chem. Phys.* **119**, 11099 (2003).

³⁷K. A. Peterson, *J. Chem. Phys.* **119**, 11113 (2003).

³⁸T. H. Dunning, Jr., *J. Chem. Phys.* **90**, 1007 (1989).

³⁹R. A. Kendall, T. H. Dunning, Jr., and R. J. Harrison, *J. Chem. Phys.* **96**, 6796 (1992).

⁴⁰T. Helgaker, W. Klopper, H. Koch, and J. Noga, *J. Comput. Phys.* **106**, 9639 (1997).

⁴¹K. T. Tang and J. P. Toennies, *J. Chem. Phys.* **80**, 3726 (1984).

⁴²R. A. Aziz and H. H. Chen, *J. Chem. Phys.* **67**, 5719 (1977).

⁴³W. H. Press, S. A. Teukolsky, W. T. Vetterling, and B. P. Flannery, *Numerical Recipes in FORTRAN. The Art of Scientific Computing*, 2nd ed. (Cambridge University Press, Cambridge, 1992).

⁴⁴D. M. Brink and G. R. Satchler, *Angular Momentum* (Clarendon, Oxford, 1968).

⁴⁵S. Green, *J. Chem. Phys.* **64**, 3463 (1976).

⁴⁶S. C. Wang, *Phys. Rev.* **34**, 243 (1929).

⁴⁷J. C. Light and T. Carrington, Jr., *Adv. Chem. Phys.* **114**, 263 (2000).

⁴⁸R. Kosloff and D. Kosloff, *J. Comput. Phys.* **63**, 363 (1986).

⁴⁹C. Leforestier and R. E. Wyatt, *J. Chem. Phys.* **78**, 2334 (1983).

⁵⁰A. Askar and A. S. Cakmak, *J. Chem. Phys.* **68**, 2794 (1978).

⁵¹J. Lv, H. Wang, L. Zheng, D. Yang, and R. Zheng, *Chem. Phys. Lett.* **687**, 31 (2017).

⁵²F. Ancilotto, M. Barranco, F. Coppens, J. Eloranta, N. Halberstadt, A. Hernando, D. Mateo, and M. Pi, *Int. Rev. Phys. Chem.* **36**, 621 (2017).

⁵³For the Wigner rotation matrices, we adopt the same phase convention as in the work of Zare.³⁴

⁵⁴Note in particular that M is always a good quantum number (J_Z is diagonal).